Rise velocities of single bubbles in a narrow channel between parallel flat plates

Hashida, Masaaki

Hayashi, Kosuke

Tomiyama, Akio

(Citation)
International Journal of Multiphase Flow,111:285-293

(Issue Date)
2019-02

(Resource Type)
journal article

(Version)
Accepted Manuscript

(URL)
https://hdl.handle.net/20.500.14094/90006119

Rise velocities of single bubbles in a narrow channel between parallel flat plates

Masaaki Hashida [a], Kosuke Hayashi [a], Akio Tomiyama [b]

[a] *Graduate School of Engineering, Kobe University, 1-1 Rokkodai, Nada, Kobe, Japan*

[b] *Corresponding author:* tomiyama@mech.kobe-u.ac.jp, TEL/FAX:*+81-78-803-6131*

Graduate School of Engineering, Kobe University, 1-1 Rokkodai, Nada, Kobe, Japan

Abstract

Effects of the bubble lateral motion and the liquid viscosity, μ_L, on the rise velocity, V_B, and the drag coefficient of a single bubble in a narrow channel were investigated. The gap thickness of the channel was 3 mm. The bubble diameter, d_B, was from 7 to 20 mm. Clean water and glycerol-water solutions were used for the liquid phase. The μ_L ranged from 0.9 to 65.7 mPa·s. Air was used for the gas phase. The conclusions obtained are as follows: (1) the bubble motion transits from zigzagging to rectilinear as d_B increases and the transition abruptly takes place at a certain critical d_B, which decreases with increasing μ_L, (2) the abrupt transition causes a stepwise increase in V_B, (3) the curvature of the bubble nose in the rectilinear regime strongly affects V_B, resulting in unavoidable scatter in V_B data in low viscosity systems due to large shape oscillation, and (4) Filella's V_B correlation for air-water systems is deducible from the force balance and applicable to high viscosity systems, provided that the model coefficient is tuned for each μ_L, implying that the drag coefficient can be expressed in terms of the Morton number and the gap-to-bubble diameter ratio.

Keywords

two-dimensional bubble, bubble lateral motion, rise velocity, viscosity effect, drag coefficient

1. Introduction

Bubbly flows in a confined channel geometry, e.g. a pipe, a cylindrical column and a narrow channel, appear in various practical systems. The channel walls may affect shapes and motion of bubbles. For example, the shape of a bubble flowing in a narrow channel between parallel plates is planar and its motion in the direction normal to the wall is restricted (Collins, 1965; Grace and Harrison, 1967; Maneri and Mendelson, 1968; Bessler and Littman, 1987; Bush and Eames, 1998; Zhang et al., 2009; Yamanoi and Kageyama, 2010; Roig et al., 2012; Filella et al., 2015; Wang et al., 2016). Understanding the dynamics of bubbles under the wall effects is of great importance in designing the practical systems.

There are several studies on bubble dynamics in a narrow channel. Collins (1965) investigated the mean rise velocity, V_B, of a single two-dimensional air bubble in water. He deduced a velocity correlation from the balance between inertial and buoyant forces, i.e. $V_B = 0.58[gd_B]^{1/2}$, where g is the magnitude of the acceleration of gravity, and d_B the circle-area-equivalent diameter of a two-dimensional bubble. This correlation shows that the bubble motion is governed by the Froude number, $V_B/[gd_B]^{1/2}$, only. Grace and Harrison (1967) and Maneri and Mendelson (1968) obtained similar velocity correlations. Roig et al. (2012) investigated the velocities of air bubbles in a narrow

channel filled with water. The bubble Reynolds number, *Re*, was found to be proportional to the Archimedes number, *Ar*, in their experiments, and they proposed the following empirical correlation:

$$Re = 0.5Ar \tag{1}$$

where $Re = \rho_L V_B d_B/\mu_L$, $Ar = [\rho_L(\rho_L-\rho_G)g d_B^3]^{1/2}/\mu_L$, ρ_L is the liquid density, ρ_G the gas density, and μ_L the liquid viscosity. Although *Re* and *Ar* account for the viscous force, Eq. (1) is equivalent to $V_B = 0.5[(\rho_L-\rho_G)g d_B/\rho_L]^{1/2}$, which does not include the viscous effects. Roig et al. classified the bubble shapes and the paths into several regimes in terms of *Ar* and pointed out that the wake structure plays an important role in the regime transition. They also found that the amplitude of the path oscillation of ellipsoidal bubbles increases with *Ar* for *Ar* smaller than a certain critical value, whereas it steeply decreases at the critical *Ar* due to the abrupt attenuation of the bubble wake. They, however, did not discuss the relation between V_B and the attenuation of path oscillation.

Filella et al. (2015) carried out experiments on bubbles in a narrow channel of $\delta = 3.1$ mm. They pointed out that their V_B data and those of Roig et al. (2012) for $\delta = 1$ mm can be well correlated by taking into account the effects of the gap thickness, i.e.

$$Re_{SE} = CAr_{SE} \tag{2}$$

or

$$Re = C(3\delta / 2d_{SE})^{1/6} Ar \tag{3}$$

where C = 0.7 and the bubble Reynolds number, Re_{SE}, and the Archimedes number, Ar_{SE}, use the sphere-volume-equivalent diameter, d_{SE} (= $[3d_B^2\delta/2]^{1/3}$) for the characteristic length. Wang et al. (2016) also investigated the effects of δ on V_B and confirmed that δ/d_B is required to correlate V_B for various δ. The above studies dealing with bubbles in water show that V_B is determined by the balance between the inertia, buoyancy and the gap effects. However, to our best knowledge, there are few studies on the effects of the liquid viscosity on V_B in a narrow channel and the viscous effect on V_B has not been well understood.

Experiments on air bubbles rising through stagnant glycerol-water solutions in a narrow channel were carried out in this study to investigate the relation between the amplitude of the path oscillation and V_B and the effects of the liquid viscosity on V_B.

2. Experimental

2.1 Experimental setup

Fig. 1 shows the experimental setup. The test section, i.e. the narrow channel of δ = 3.0±0.1 mm, was made of transparent acrylic resin. Its width and height were 200 and 620 mm, respectively. The stainless nozzle for injecting single bubbles was located at the bottom of the test section. The inner diameter of the nozzle was 2.0 mm. The x and z are the horizontal and vertical coordinates, and their origin is set at the nozzle tip. The test section was filled with liquid at room temperature (298±0.5 K) and atmospheric pressure up to z = 500 mm.

Clean water (Millipore, Elix 3.0) and glycerol-water solutions were used for the liquid phase. The glycerol mass concentration, C_{GL}, was varied from 0.21 to 0.83. The ρ_L and μ_L of clean water and the glycerol-water solutions and the surface tensions, σ, are summarized in **Table 1**, in which M is the Morton number defined by

$$M = \frac{\mu_L^4 (\rho_L - \rho_G) g}{\rho_L^2 \sigma^3} \tag{4}$$

The ρ_G and the gas viscosity, μ_G, were 1.2 kg/m^3 and 1.8×10^{-3} Pa·s, respectively. The ρ_L, μ_L and σ were measured by using a densimeter (Ando Keiki Co., Ltd., JIS B7525), a viscometer (A&D Co., Ltd., SV-10) and the pendant bubble method (Lin et al., 1990; Pan et al., 1998), respectively. The uncertainties in ρ_L, μ_L and σ estimated at 95% confidence were 0.02%, 4.2% and 3.3%, respectively.

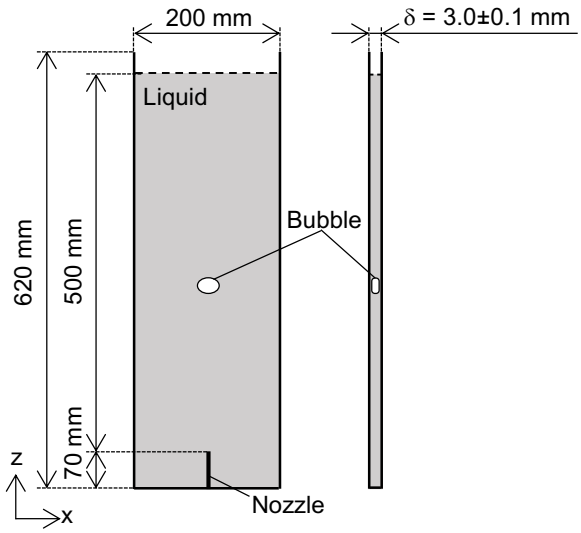

Fig. 1 Experimental setup

Table 1 Liquid properties (298±0.5 K)

	C_{GL}	μ_L [mPa·s]	ρ_L [kg/m^3]	σ [N/m]	log$M$
Glycerol-water solution	0.21	1.7	1047	0.071	-9.6
	0.38	3.1	1087	0.069	-8.6
	0.67	13.5	1167	0.066	-6.0
	0.83	65.7	1213	0.065	-3.3
Clean water	0	0.9	997	0.072	-10.8

2.2 Measurement method

The diameter and rise velocity of a single bubble were measured by processing bubble images. Successive images were taken by using a high-speed video camera (Photron Ltd., FASTCAM SA-X2) (**Fig. 2(a)**). The spatial and temporal resolutions were 0.20 mm/pixel and 1/125 s, respectively. A fluorescent light was used for back illumination. The projected area, $A(z)$, of a bubble and the instantaneous rise velocity, $V(z)$, were measured by using an image processing method (Hosokawa and Tomiyama, 2003) (**Fig. 2(b)**). The bubble diameter, $d(z)$, was calculated as

$$d(z) = \sqrt{\frac{4A(z)}{\pi}} \tag{5}$$

The mean bubble diameter, d_B, was evaluated by averaging $d(z)$ for $300 \leq z \leq 400$ mm.

The uncertainty in d_B estimated at 95% confidence was less than 2%. The range of d_B was from 7 to 20 mm. The geometric center, $x_g(z)$, of a bubble was also obtained (**Fig. 2(c)**). The $V(z)$ was calculated from the traveling distance in the z direction during the time duration between two successive images. **Fig. 3** shows $V(z)$ of a small bubble (d_B = 9 mm) and that of a large bubble (d_B = 18.5 mm). The $V(z)$ of the small bubble periodically fluctuated due to the path oscillation, and therefore, V_B was obtained by averaging $V(z)$ for three periods. The $V(z)$ of the large bubble was almost constant since the bubble path was almost rectilinear, and therefore, V_B was obtained by averaging $V(z)$ for $300 \leq z \leq 400$ mm.

Fig. 4 shows a bubble with zigzagging motion and the path of the geometric center (dotted line). The mean path (solid line), (x_c, z_c), of the center of a bubble was obtained as a linear function

$$x_c = az_c + b \tag{6}$$

by using the least square fit, where a and b are constants. The $\phi(z)$ in the figure is the distance between the mean path and the geometric center calculated by

$$\phi(z) = \frac{\left| az - x_g(z) + b \right|}{\sqrt{a^2 + 1}} \tag{7}$$

The standard deviation, s, from the mean path was calculated by

$$s = \sqrt{\frac{1}{z_2 - z_1} \int_{z_1}^{z_2} \phi(z)^2 \, dz} \tag{8}$$

where z_1 and z_2 are 300 and 400 mm, respectively. The s will be used as an indicator of the amplitude of the path oscillation in the following sections.

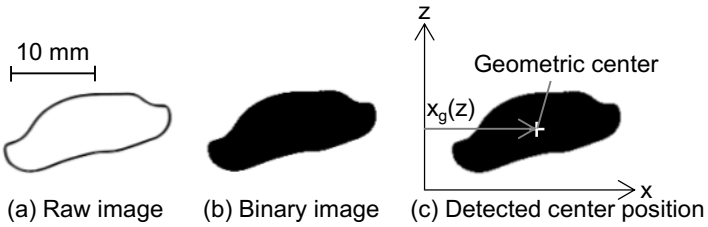

Fig. 2 Image processing for measurements of A and geometric center of bubble

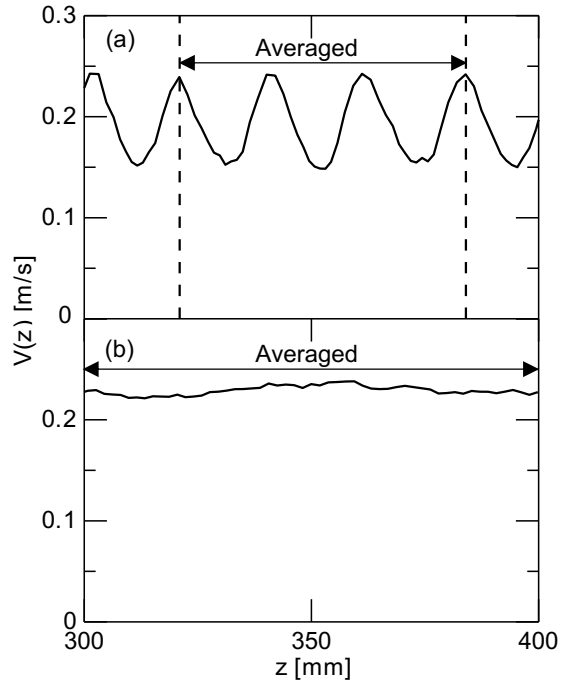

Fig. 3 Instantaneous velocities at (a) d_B = 9 and (b) 18.5 mm

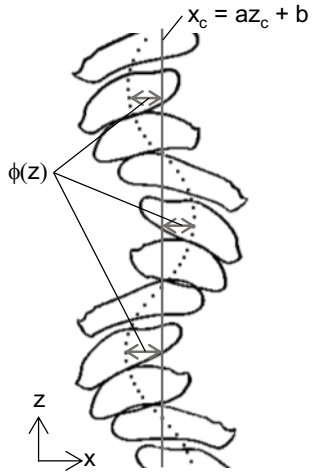

Fig. 4 Evaluation method of bubble lateral motion

3. Results and discussion

3.1 Bubble shape and velocity

Fig. 5 shows V_B at C_{GL} = 0.38. The V_B increases with increasing d_B up to $d_B \sim 8$ mm, whereas for $8 < d_B < 10$ mm V_B is almost constant. The V_B decreases with increasing d_B for $10 < d_B < 12$ mm, and then, V_B abruptly increases at $d_B \sim 12$ mm. The V_B again increases with increasing d_B for larger bubbles. This complex and interesting trend has not been discussed in previous studies (Filella et al., 2015; Krishna et al., 2000; Piedra et al., 2015; Roig et al., 2012; Wang et al., 2014; Wang et al., 2016), and V_B has been correlated as a monotonically increasing function of d_B in all the ranges of d_B (Collins, 1965; Filella et al., 2015; Roig et al., 2012).

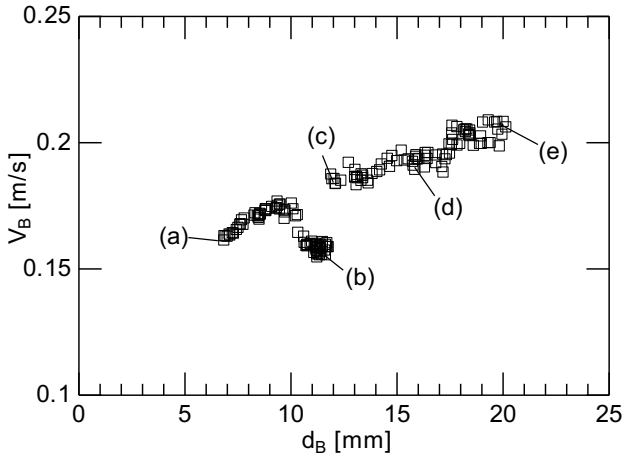

Fig. 5 V_B in glycerol-water solution of C_{GL} = 0.38

Fig. 6 shows motion of bubbles and their paths at C_{GL} = 0.38, where (a)–(e) are the data for those in **Fig. 5**. The bubble shape at d_B = 7.0 mm (**Fig. 6(a)**) is distorted ellipsoidal and its bubble path (dotted line) is zigzag. The shape deformation and the amplitude of zigzag path increase with increasing d_B as shown in **Fig. 6(b)** (d_B = 11.7 mm). The bubble diameters in **Figs. 6(b)** and **(c)** are almost the same, whereas the bubble lateral motion at d_B = 12.1 mm is much smaller. The shapes of the larger bubbles in **Figs. 6(d)** and **(e)** are cap and their paths are almost rectilinear. **Fig. 7** shows s of bubbles at C_{GL} = 0.38. The s is almost constant up to d_B = 7.5 mm, whereas for 7.5 < d_B < 12 mm s increases with increasing d_B. Then s abruptly decreases. Comparing this trend of s with that of V_B in **Fig. 5** reveals that the complex trend of V_B is obviously related with the bubble lateral motion, i.e. the increase in s (enhancement in zigzagging motion) makes V_B constant or decreases V_B and the abrupt decrease in s (transition from zigzagging to rectilinear) causes a jump in V_B. The small V_B of bubbles with the zigzagging motion must be due to the use of the potential energy for lateral motion.

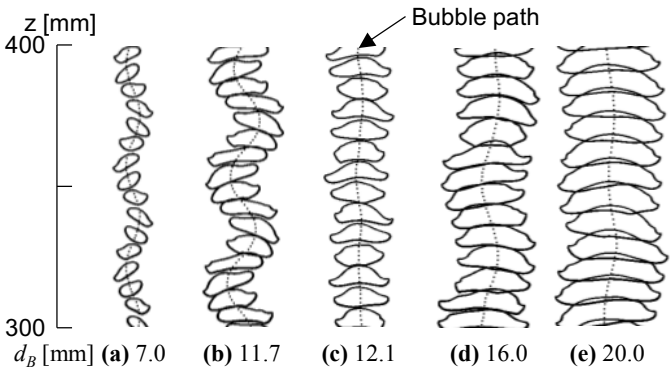

Fig. 6 Bubble motion and path at C_{GL} = 0.38

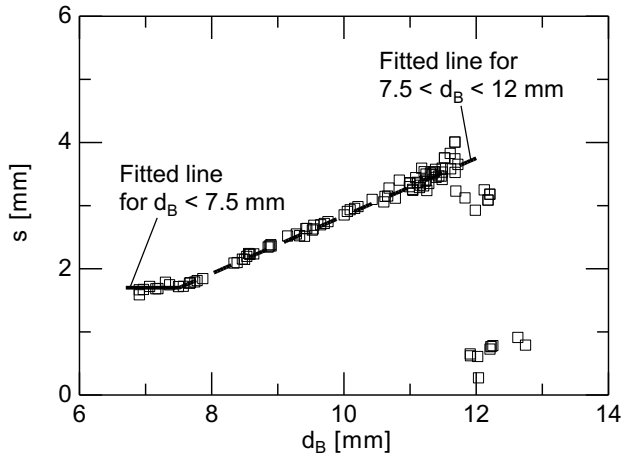

Fig. 7 s of bubbles at C_{GL} = 0.38

Bubble shapes in the glycerol-water solutions of various concentrations are summarized in **Fig. 8**. The paths of the bubbles in **Figs. 8(a)**, **(b)**, **(f)** and **(g)** (C_{GL} = 0.21 and 0.38) are zigzag, whereas those of the larger bubbles (**(c)–(e)** and **(h)–(j)**) are almost rectilinear. The bubbles at C_{GL} = 0.67 also show the transition from zigzagging to rectilinear (**(k)–(o)**) although the increase in μ_L makes capillary waves very weak. On the other hand, all the bubbles at C_{GL} = 0.83 rise rectilinearly (**(p)–(t)**) due to strong viscous damping on shape oscillation.

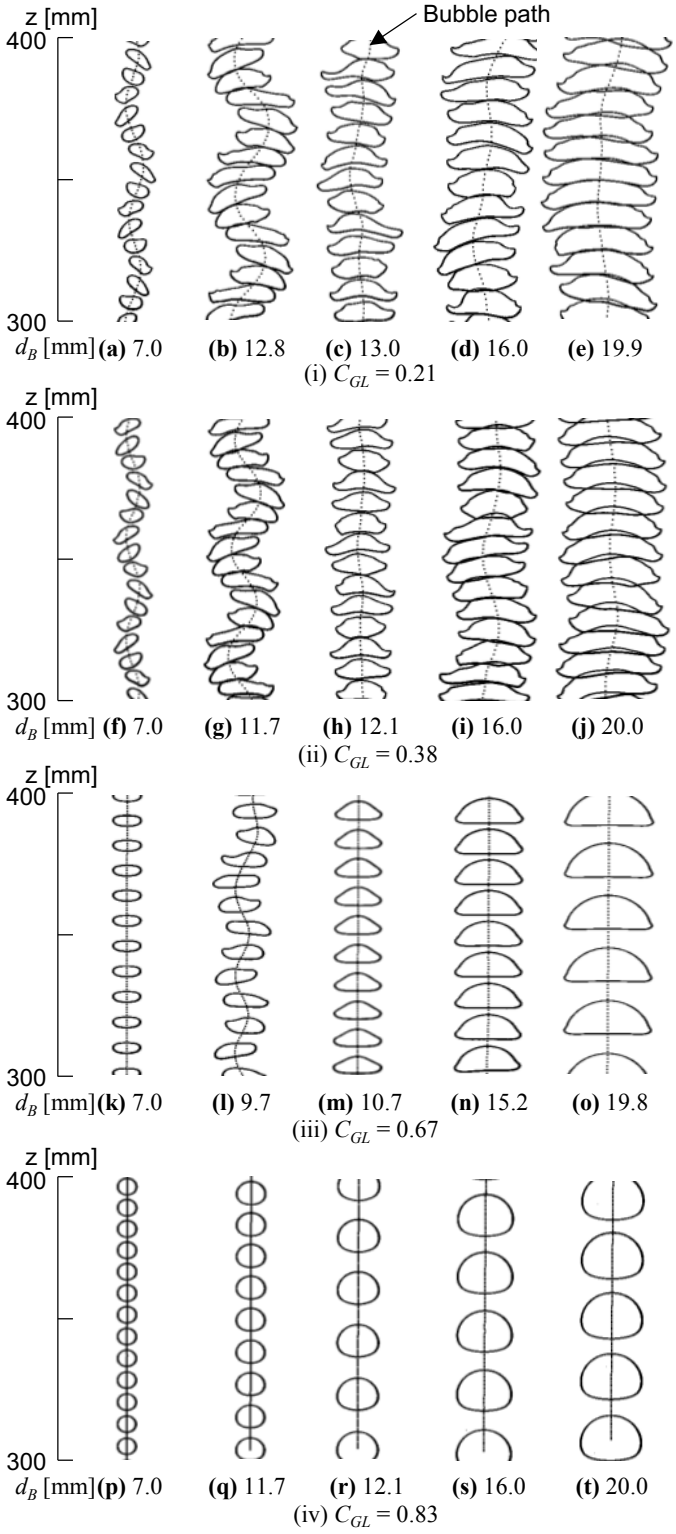

Fig. 8 Bubble motion and path in glycerol-water solutions

Fig. 9 shows s of bubbles in the glycerol-water solutions. The s increases with increasing d_B except for C_{GL} = 0.83. The s also abruptly decreases at certain critical diameters. The critical d_B are about 13, 12 and 11 mm at C_{GL} = 0.21, 0.38 and 0.67, respectively. The increase in μ_L thus lowers the critical diameter. In the zigzagging path regime (for d_B less than the critical diameter), there is no difference in s between C_{GL} = 0.21 and 0.38. Further increase in C_{GL} causes reduction of s, and s is almost zero at C_{GL} = 0.83, i.e. the viscous force strongly attenuates the lateral fluctuation of bubble motion.

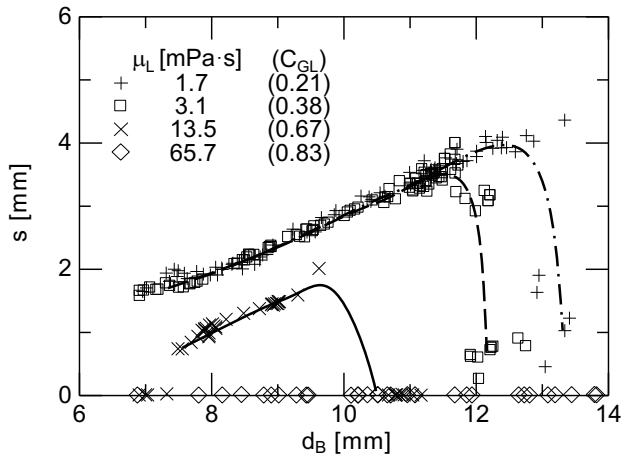

Fig. 9 s of bubbles in glycerol-water solutions

Fig. 10 shows V_B in the glycerol-water solutions, where (a)–(t) are the data for those in **Fig. 8**. The V_B decreases with increasing μ_L. The d_B for the abrupt increase in V_B agree with those for the abrupt decrease in s, again confirming the strong relation between V_B and the bubble lateral motion.

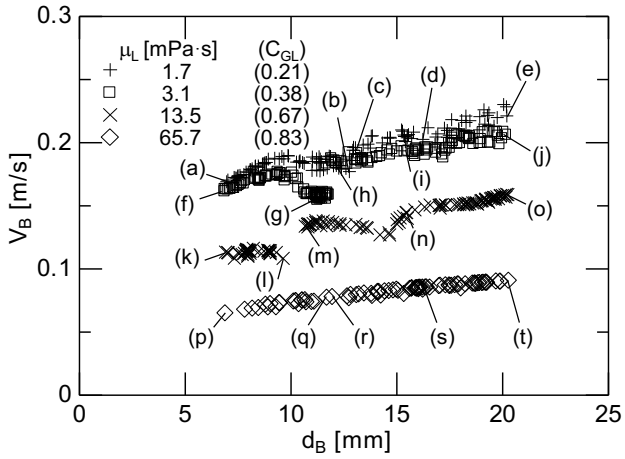

Fig. 10 V_B in glycerol-water solutions

There is another abrupt change in V_B at $d_B \sim 15$ mm in the case of $C_{GL} = 0.67$ as clearly seen in **Fig. 11**. **Fig. 12** shows s, which is very small except at $d_B \sim 15$ mm. The bubble paths at $d_B = 12.2$, 14.6 and 15.8 mm shown in **Fig. 12** are almost rectilinear, and therefore, the cause of the secondary velocity jump is not the transition of the bubble motion from zigzagging to rectilinear. The largest s however corresponds to d_B at the velocity jump. This is due to the slight lateral shift of the rectilinear path as will be explained later. The shapes of bubbles of $d_B = 12.2$, 14.6 and 15.8 mm are compared in **Fig. 13**. As is well known the nose shape is the primal factor in bubble velocity (Tomiyama et al., 2002), and therefore, the transition in the nose shape could be attributed to the cause of the secondary velocity jump. The following data of the bubble having the largest s strongly support this speculation. **Fig. 14** shows the bubble of 14.7 mm, whose path is rectilinear but suddenly shifts toward the right side. This shift of the path is accompanied by the nose shape transition from small to large curvature regimes and caused the largest s shown in **Fig. 12**. The V_B in the large curvature region ($z > 410$ mm) is 0.138 m/s, which is 4% faster than that (0.132 m/s) in the small curvature region ($z < 340$ mm). Bubbles with large curvature can therefore rise faster than those with

small curvature. The bubble shape and path seem to be stable for z < 340 mm and the transition takes place without any indication, implying that the mode of the bubbles with small curvature is less stable than that of the bubbles with large curvature and the transition can be caused even with small perturbation. The transition would easily occur in low μ_L systems since viscous damping on perturbations is weak at low μ_L.

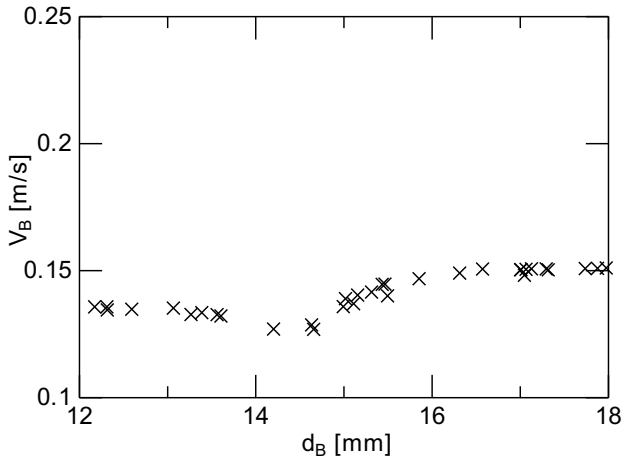

Fig. 11 V_B at C_{GL} = 0.67

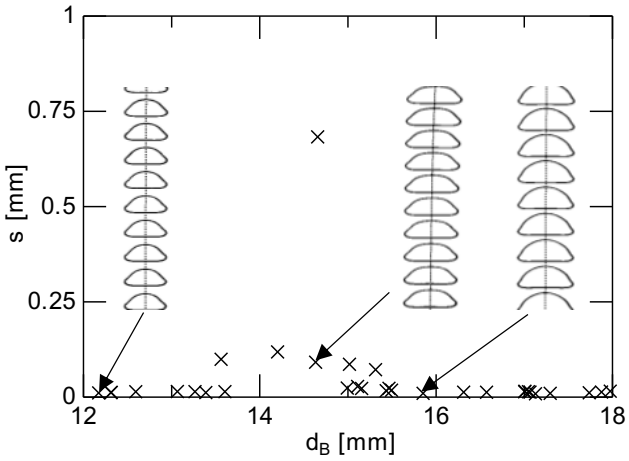

Fig. 12 s of bubbles at C_{GL} = 0.67

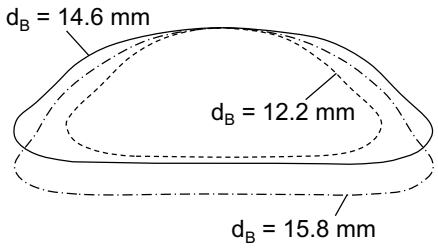

Fig. 13 Bubble shapes at d_B = 12.2, 14.6 and 15.8 mm at C_{GL} = 0.67

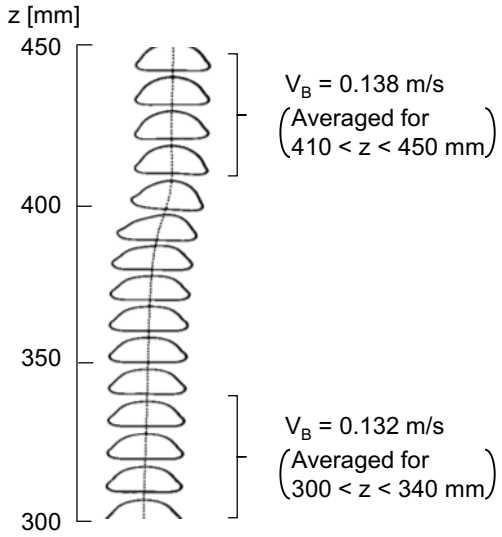

Fig. 14 Shape and path of bubble of d_B = 14.7 mm

Fig. 15 shows bubbles at C_{GL} = 0 (clean water). The path transition from zigzagging to rectilinear also takes place as Roig et al. (2012) pointed out. **Figs. 16** and **17** show V_B and s of bubbles at C_{GL} = 0. The V_B increases with d_B for $d_B \lesssim 10$ mm, for which s increases. The increasing rate of s becomes larger for $10 \lesssim d_B \lesssim 14$ mm, resulting in almost constant V_B. The data of s in Regime 1 agreed well with those evaluated from the bubble paths given in Filella et al. (2015). The abrupt decrease in s at about 14 mm corresponds to the path transition from zigzagging to rectilinear, and V_B again increases with d_B for $d_B \gtrsim 14$ mm. However the V_B data in the rectilinear regime largely scatter.

The scatter might be due to the fluctuation of the nose shape (**Figs. 15(d)** and **(e)**). The large fluctuation of the nose shape would be the nature of bubbles in low liquid viscosity systems and can also be attributed to an initial disturbance applied at the injection of the gas phase from the syringe. As reported in Tomiyama et al. (2002) for three-dimensional bubbles in the surface-tension-force dominant regime, the initial disturbance in gas injection drastically affects the bubble motion and realizes various rise velocities even at the same bubble diameter. Filella's velocity data of bubbles in water (Filella et al., 2015) also show large scatter for $d_B \gtrsim 10$ mm and non-monotonous velocity dependence on d_B though they did not remark this dependence.

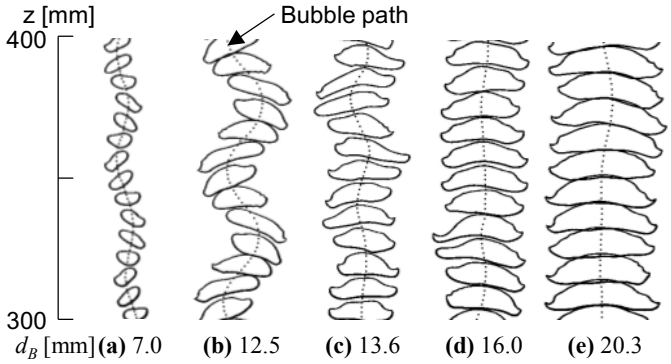

Fig. 15 Bubble motion and path at $C_{GL} = 0$ (clean water)

3.2 Comparisons between V_B data and velocity correlations

Filella et al. (2015) experimentally investigated the effects of δ on V_B. They reported that V_B of air bubbles in water at δ = 1 and 3.1 mm can be well correlated using Eq. (2). The Re_{SE} and Ar_{SE} are defined by

$$Re_{SE} = \frac{\rho_L V_B d_{SE}}{\mu_L} \tag{9}$$

$$Ar_{SE} = \frac{\sqrt{\rho_L (\rho_L - \rho_G) g d_{SE}^3}}{\mu_L} \tag{10}$$

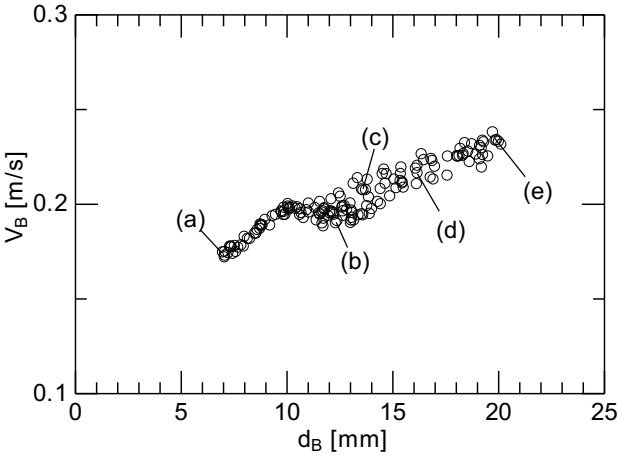

Fig. 16 V_B at $C_{GL} = 0$ (clean water)

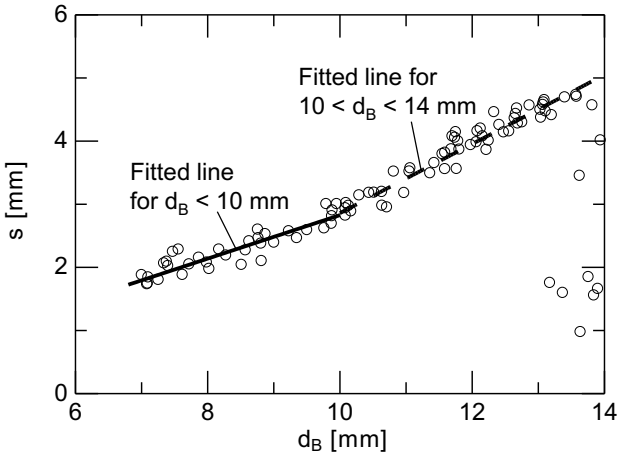

Fig. 17 s of bubbles at $C_{GL} = 0$ (clean water)

The functional form of Eq. (2) can be deduced from the balance between the buoyant and drag forces as will be discussed later, and therefore, Eq. (2) would be reliable. Eq. (2) can be rewritten as

$$V_B = C\left(\frac{3}{2}\frac{\delta}{d_B}\right)^{\frac{1}{6}}\sqrt{\frac{(\rho_L - \rho_G)gd_B}{\rho_L}} \tag{11}$$

Eq. (11) is compared with the data in **Fig. 18**. Although Eq. (11) expresses well the trend of V_B, the characteristics of V_B in the path transition regime ($10 \lesssim d_B \lesssim 14$ mm) are not predictable. The correlation gives good evaluations of V_B of bubbles of zigzagging motion (Regime 1: $d_B < 10$ mm), whereas C should be varied from 0.65 to 0.70 to cover the V_B data of bubbles of rectilinear motion (Regime 2: $d_B \gtrsim 14$ mm). Fitting Eq. (11) to the data yields $C = 0.71$ and 0.67 in Regime 1 and 2, respectively, with which we can obtain better evaluations as shown in the figure.

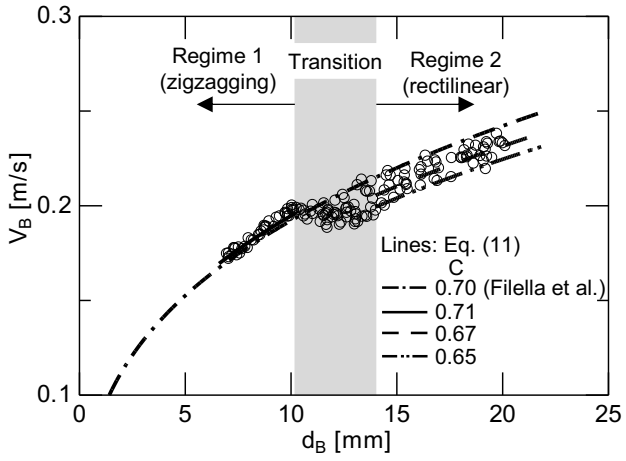

Fig. 18 Comparison between V_B data at $C_{GL} = 0$ and Eq. (11)

Figs. 19(a) and **(b)** show relations between Re_{SE} and Ar_{SE} in Regime 1 and 2, respectively. The classification of the path regimes in glycerol-water solutions is given in Appendix A. The Re_{SE} are proportional to Ar_{SE}. Filella's functional form can therefore be applicable even for high viscosity liquids. However C must be tuned for C_{GL}. Eq. (2) with C tuned for C_{GL} is compared with the data in **Fig. 20**. The agreements are good. The C decreases with increasing C_{GL} (μ_L).

The ranges of the dimensionless groups, i.e. Re, Ar, Re_{SE}, Ar_{SE} and $Re(\delta/d_B)^2$, are summarized in **Table 2**, where $Re(\delta/d_B)^2$ is the gap Reynolds number (Bush and Eames, 1998). Bubbles are in the viscous force dominant regime when $Re(\delta/d_B)^2 << 1$ while in the inertial force dominant regime when $Re(\delta/d_B)^2 >> 1$. The range of $Re(\delta/d_B)^2$ at C_{GL} = 0.83 is from 0.8 to 1.6. Hence the dynamics of bubbles under this condition is mainly governed by the viscous force, which would be the reason why only rectilinear motion of bubbles was observed.

Table 2 Ranges of dimensionless groups

C_{GL}	Re	Ar	Re_{SE}	Ar_{SE}	$Re(\delta/d_B)^2$
0.21	770-3020	1188-5880	666-1770	956-2775	65-143
0.38	390-1463	630-3150	338-889	508-1487	32-74
0.67	68-278	155-780	59-168	125-368	6.1-13
0.83	8.3-34	33-167	7.2-21	27-79	0.8-1.6
0	1349-5203	2037-9933	1170-3180	1632-4692	113-248

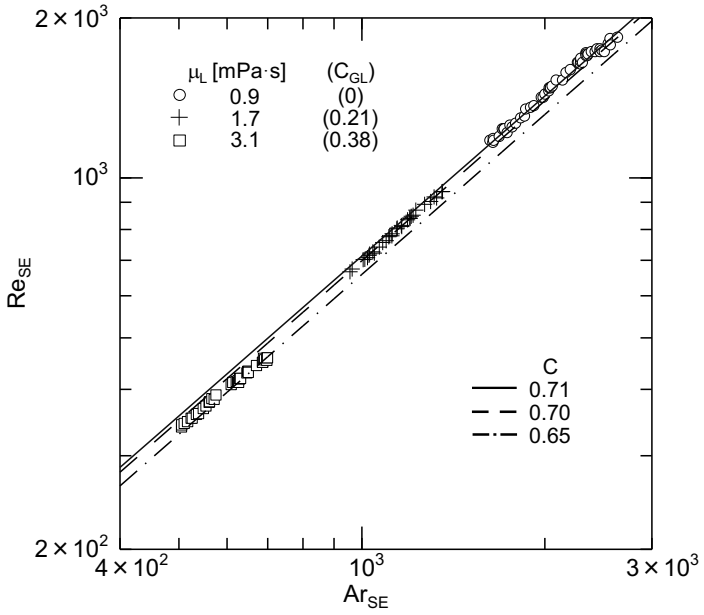

(a) Regime 1 (No bubbles were in Regime 1 for $C_{GL} \geq 0.67$)

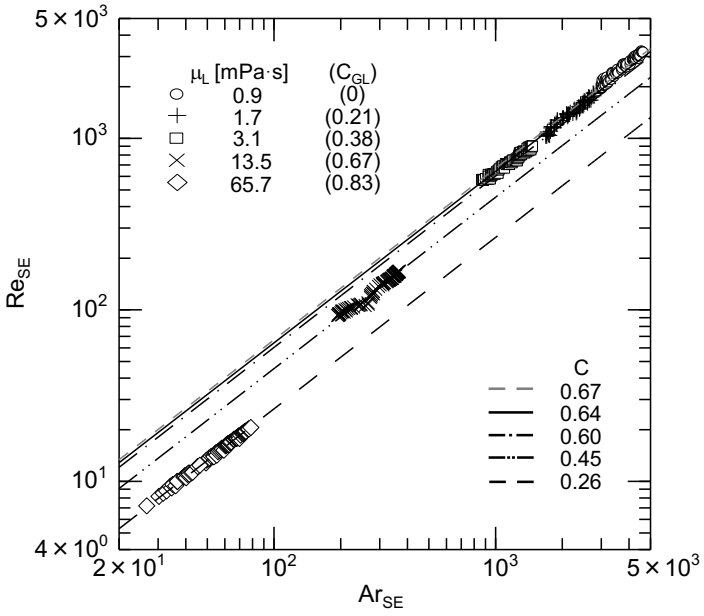

(b) Regime 2

Fig. 19 Re_{SE} plotted against Ar_{SE}

3.3 Drag coefficient

The V_B decreases with increasing μ_L, in other words, the drag force increases with increasing μ_L. The balance between the buoyant and drag forces is given by

$$\frac{C_D}{2}\rho_L V_B^2 d_B \delta = (\rho_L - \rho_G) g \frac{\pi}{4} d_B^2 \delta \tag{12}$$

where C_D is the drag coefficient. Solving Eq. (12) for C_D yields

$$C_D = \frac{\pi(\rho_L - \rho_G) g d_B}{2\rho_L V_B^2} \tag{13}$$

The C_D increases with increasing Re_{SE} as shown in **Fig. 20**, confirming that C_D cannot be correlated in terms of Re_{SE}.

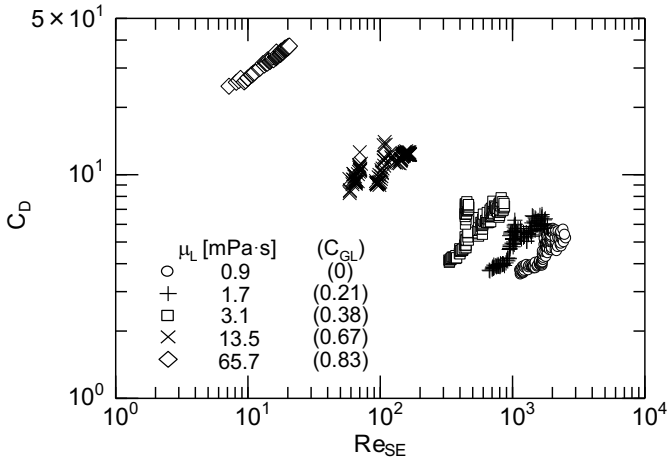

Fig. 20 C_D plotted against Re_{SE}

Rearranging Eq. (12) by using dimensionless groups yields

$$Re_{SE} = \frac{1}{\sqrt{C_D}} \left(\frac{\pi^2}{6} \frac{d_{SE}}{\delta} \right)^{\frac{1}{4}} Ar_{SE} \tag{14}$$

whose functional form is the same as that of Eq. (2) when C_D is given by $C_D = (d_{SE}/\delta)^{1/2}$. Comparing this equation with Eq. (2) gives

$$C = \frac{1}{\sqrt{C_D}} \left(\frac{\pi^2}{6} \frac{d_{SE}}{\delta} \right)^{\frac{1}{4}} \tag{15}$$

As discussed in Sec. 3.2, C depends on C_{GL}, in other words, on the fluid properties or the Morton number, M. Since d_{SE}/δ does not affect C, C_D may be written as

$$C_D = \frac{1}{f(M)} \left(\frac{d_{SE}}{\delta} \right)^{\frac{1}{2}} \tag{16}$$

where $f(M)$ is a function of M. Substituting Eq. (16) into Eq. (15) yields

$$C = f(M)^{\frac{1}{2}} \left(\frac{\pi^2}{6} \right)^{\frac{1}{4}} \tag{17}$$

The values of $f(M)$ evaluated using the experimental data are shown in **Fig. 21**. The $f(M)$

decreases with increasing M in both regimes and can be fitted as

$$f(M) = \begin{cases} \left(C_1 - C_2 \tanh(C_3 \log(M + C_{R1}))\right)^{C_4} & \text{for Regime 1} \\ \left(C_1 - C_2 \tanh(C_3 \log(M))\right)^{C_4} & \text{for Regime 2} \end{cases} \tag{18}$$

where $C_1 = 0.824$, $C_2 = 0.146$, $C_3 = -0.168$, $C_4 = 27$ and $C_{R1} = 0.33$. The fitting equation gives good evaluations of V_B as shown in **Fig. 22**, and therefore, the assumption, Eq. (16), is reasonable at least in the present experimental range. Comparisons between the empirical correlation and all the V_B data are given in Appendix B.

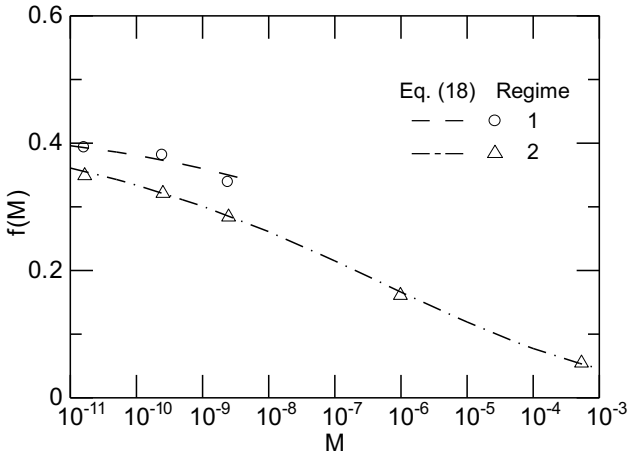

Fig. 21 $f(M)$ plotted against M

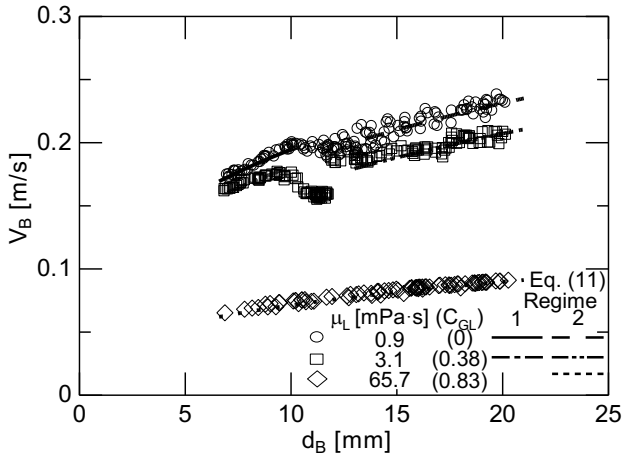

Fig. 22 Comparison between V_B data and $Re_{SE} = CAr_{SE}$ with Eq. (16)

4. Conclusion

The mean rise velocities, V_B, and drag coefficients of single bubbles in stagnant liquids in a narrow channel were measured to investigate the effects of bubble lateral motion and the liquid viscosity on V_B and the drag coefficient. The gap, δ, of the narrow channel was 3 mm. The bubble diameter, d_B, was varied from 7 to 20 mm. The gas phase was air. Clean water and glycerol-water solutions were used for the liquid phase. The glycerol mass concentration, C_{GL}, was from 0.21 to 0.83. The conclusions obtained under the present experimental conditions are as follows:

(1) The bubble motion transits from zigzagging to rectilinear as the bubble diameter increases. The transition abruptly takes place at a certain critical bubble diameter, which decreases with increasing the liquid viscosity.

(2) The abrupt transition in the bubble motion from zigzagging to rectilinear causes a stepwise increase in the rise velocity.

(3) In the rectilinear path regime, there are a high-velocity mode and a low-velocity mode depending on the bubble nose shape even at the same bubble size. The curvature of the nose of a bubble in the former is larger than in the latter. Large shape oscillations in low viscosity liquids therefore induce unavoidable scatter in velocity data because of unstable nose shape.

(4) The functional form of the velocity correlation for air-water systems proposed by Filella et al. is applicable to high viscosity systems, provided that the coefficient is tuned for each liquid viscosity. This fact means the drag coefficient can be expressed in terms of the Morton number and the gap-to-bubble diameter ratio.

(5) Fillela's rise velocity correlation is deducible from the balance between the drag and buoyant forces by setting $C_D = (d_{SE}/\delta)^{1/2}$, where C_D is the drag coefficient, d_{SE} the sphere-volume-equivalent bubble diameter, and δ the gap thickness.

Appendix

A. Path regime classification

The experimental data of the mean rise velocity, V_B, in glycerol-water solutions are shown in **Fig. A1**, in which Regime 1 and 2 represent the zigzagging and rectilinear motions of bubbles, respectively.

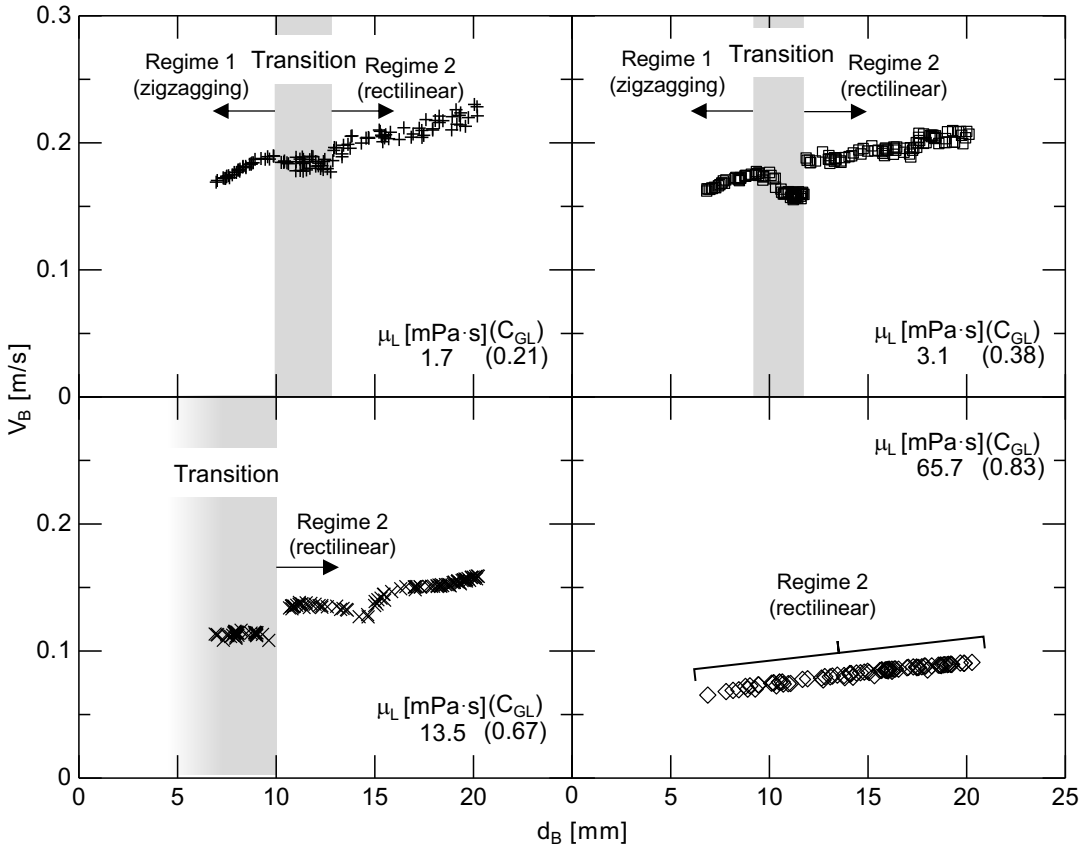

Fig. A1 V_B in glycerol-water solutions

B. Comparisons between empirical velocity correlation and experimental data

Comparisons between Eq. (11) and V_B are shown in **Fig. B1**. The coefficients, C, are calculated using Eqs. (17) and (18). The empirical correlation gives good evaluations for all the conditions.

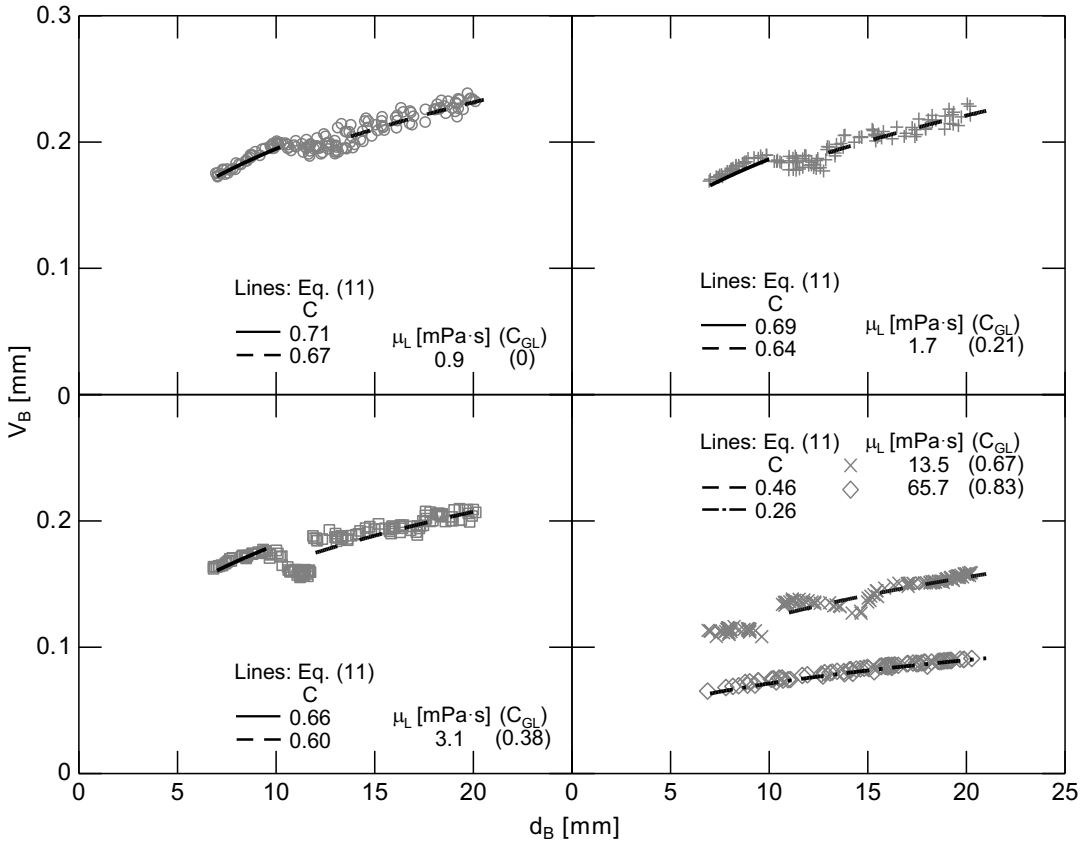

Fig. B1 Comparisons between V_B and Eq. (11) with Eqs. (17) and (18)

References

Bessler, W.F., Littman, H., 1987. Experimental studies of wakes behind circularly capped bubbles. J. Fluid. Mech. 185, 137–151.

Bush, J.W.M., Eames, I., 1998. Fluid displacement by high Reynolds number bubble motion in a thin gap. Int. J. Multiph. Flow. 24, 411–430.

Collins, R., 1965. A simple model of the plane gas bubble in a finite liquid. J. Fluid Mech. 22, 763–771.

Filella, A., Ern, P., Roig, V., 2015. Oscillatory motion and wake of a bubble rising in a thin-gap cell. J. Fluid Mech. 778, 60–88.

Grace, J.R., Harrison, D., 1967. The influence of bubble shape on the rising velocities of

large bubbles. Chem. Eng. Sci. 22, 1337–1347.

Hosokawa, S., Tomiyama, A., 2003. Lateral force acting on a deformed single bubble due to the presence of wall. Trans. Jpn. Soc. Mech. Eng., Ser. B, 69, 2214–2220 in Japanese.

Krishna, R., Baten, J.M., Urseanu, M.I., Ellenberger, J., 2000. Rise velocity of single circular-cap bubbles in two-dimensional beds of powders and liquids. Chem. Eng. Processing 39, 433–440.

Lin, S.Y., Mckeigue, K., Maldarelli, C., 1990. Diffusion-controlled surfactant adsorption studied by pendant drop digitization. AIChE J. 36, 1785–1795.

Maneri, C.C., Mendelson, H.D., 1968. The rise velocity of bubbles in tubes and rectangular channels as predicted by wave theory. AIChE J. 14, 295–300.

Pan, R., Green, J., Maldarelli, C., 1998. Theory and experiment on the measurement of kinetic rate constants for surfactant exchange at an air/water interface. J. Colloid Interface Sci. 205, 213–230.

Piedra, S., Ramos, E., Herrera, J.R., 2015. Dynamics of two-dimensional bubbles. Phys. Rev. E 91, 063013.

Roig, V., Roudet, M., Risso, F., Billet, A.M., 2012. Dynamics of a high-Reynolds-number bubble rising within a thin gap. J. Fluid Mech. 707, 444–466.

Tomiyama, A., Celata, G.P., Hosokawa, S., Yoshida, S., 2002. Terminal velocity of single bubbles in surface tension force dominant regime. Int. J. Multiph. Flow 28, 1497–1519.

Wang, X., Klaasen, B., Degrève, J., Blanpain, B., Verhaeghe, F., 2014. Experimental and numerical study of buoyancy-driven single bubble dynamics in a vertical Hele-Shaw cell. Phys. Fluids 26, 1–18.

Wang, X., Klaasen, B., Degrève, J., Mahulkar, A., Heynderickx, G., Reyniers, M.F., Blanpain, B., Verhaeghe, F., 2016. Volume-of-fluid simulations of bubble dynamics in a vertical Hele-Shaw cell. Phys. Fluids 28, 1–13.

Yamanoi, I., Kageyama, K., 2010. Evaluation of bubble flow properties between flat sheet membranes in membrane bioreactor. J. Membr. Sci. 360, 102–108.

Zhang, K., Cui, Z., Field, R.W., 2009. Effect of bubble size and frequency on mass transfer in flat sheet MBR. J. Membr. Sci. 332, 30–37.